APL Photonics

RESEARCH ARTICLE | JANUARY 28 2025

Fabrication of periodically poled lithium niobate waveguides for broadband nonlinear photonics

Furkan Ayhan ; Markus Ludwig ; Tobias Herr ; Victor Brasch ; Luis Guillermo Villanueva

APL Photonics 10, 016118 (2025)
https://doi.org/10.1063/5.0227255

View Online
Export Citation

Articles You May Be Interested In

Simulating supercontinua from mixed and cascaded nonlinearities

APL Photonics (March 2023)

Optimizing the efficiency of a periodically poled LNOI waveguide using *in situ* monitoring of the ferroelectric domains

Appl. Phys. Lett. (March 2020)

Stable and compact RF-to-optical link using lithium niobate on insulator waveguides

APL Photonics (December 2021)

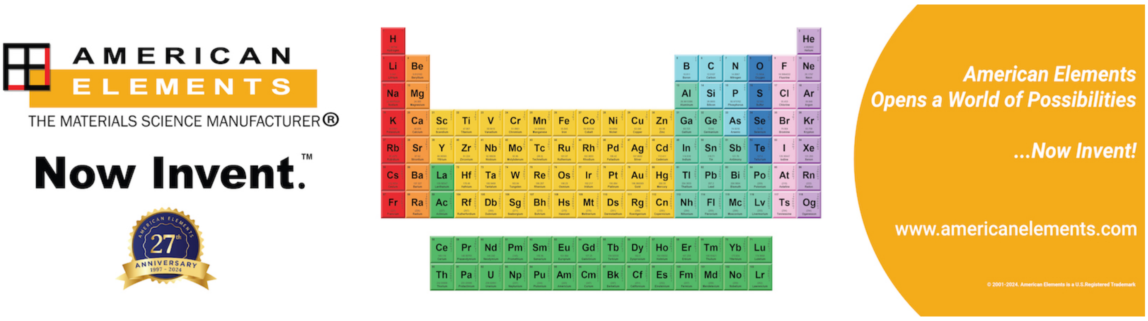

AIP Publishing

APL Photonics ARTICLE pubs.aip.org/aip/app

Fabrication of periodically poled lithium niobate waveguides for broadband nonlinear photonics

Cite as: APL Photon. 10, 016118 (2025); doi: 10.1063/5.0227255
Submitted: 8 July 2024 • Accepted: 29 December 2024 •
Published Online: 28 January 2025

Furkan Ayhan,[1,a)] **Markus Ludwig,**[2] **Tobias Herr,**[2,3] **Victor Brasch,**[4] **and Luis Guillermo Villanueva**[1,a)]

AFFILIATIONS

[1] École Polytechnique Fédérale de Lausanne (EPFL), 1015 Lausanne, Switzerland
[2] Deutsches Elektronen-Synchrotron DESY, 22607 Hamburg, Germany
[3] Physics Department, Universität Hamburg UHH, 22607 Hamburg, Germany
[4] Q.ANT GmbH, 70565 Stuttgart, Germany

[a)] **Authors to whom correspondence should be addressed:** furkan.ayhan@epfl.ch and guillermo.villanueva@epfl.ch

ABSTRACT

Nonlinear optics is the precursor for many of the modern-day applications of photonics, including femtosecond pulse synthesis, precision spectroscopy, and metrology. In the last decade, nanophotonic waveguides have not only boosted the efficiencies of nonlinear effects but also unlocked new degrees of freedom in the design process and enabled the monolithic integration of multiple nonlinear devices. Now, the advent of thin-film variants of platforms with a strong second-order nonlinearity such as lithium niobate-on-insulator (LNOI) enables entirely new applications while further improving efficiency for the existing ones. However, suitable fabrication processes are needed to exploit the full potential of these new platforms. Here, we introduce a process for fabricating high-confinement lithium niobate waveguides with periodic poling. Our waveguide designs enable both third-order nonlinear $\chi^{(3)}$ broadening and sum frequency generation (SFG) up to the fourth harmonic through a quasi-phase-matched $\chi^{(2)}$ section. In supercontinuum (SC) experiments, our devices produce multi-octave SC spectra when pumped with an 80 fs mode-locked laser at 1560 nm.

I. INTRODUCTION

While nonlinear photonics is used in many experiments and applications, supercontinuum (SC) generation stands out among them as it utilizes several different nonlinear effects over a very large bandwidth. Furthermore, the resulting broadband spectra are key enablers for many optical applications ranging from frequency combs to spectroscopy and telecom. Therefore, SC generation is a suitable setting to highlight and compare the capabilities of nonlinear photonic platforms. Over the past few decades, multiple platforms have contributed to advancements in SC generation.

First observed in bulk materials,[1,2] SC generation only revealed its full potential when used in fibers, which enabled, for example, octave-spanning coherent spectra, which were the prerequisite for self-referenced optical frequency combs.[3,4] This advancement is made possible because, in fibers, mode sizes are generally smaller and maintained over long propagation distances compared to bulk materials, thus substantially increasing the effective nonlinearity. Furthermore, by changing material compositions and fiber geometries, one can modify the chromatic dispersion (dispersion engineering) to reach the regime where the nonlinear broadening is particularly efficient (anomalous dispersion).[3,5] More recently, nanophotonic waveguides have emerged as another promising platform, for which many more materials are available with substantially larger nonlinearities.[6] The effective mode size is further reduced [Fig. 1(a)] and the cross-section of the waveguide can be adjusted or even varied over short distances of several millimeters along the propagation direction. This variability is a degree of freedom that was barely available in optical fibers, thus enabling an even higher degree of control over the intricate SC processes.

In a next technological leap, using materials with second-order ($\chi^{(2)}$) nonlinearity for nanophotonic waveguides, the SC generation does not only rely on third-order ($\chi^{(3)}$) processes, such as self-phase modulation (SPM) and four-wave mixing (FWM) anymore. Instead, more efficient $\chi^{(2)}$ processes such as second-harmonic generation (SHG), sum-frequency generation (SFG), and difference-frequency generation (DFG) can complement $\chi^{(3)}$ processes to achieve much

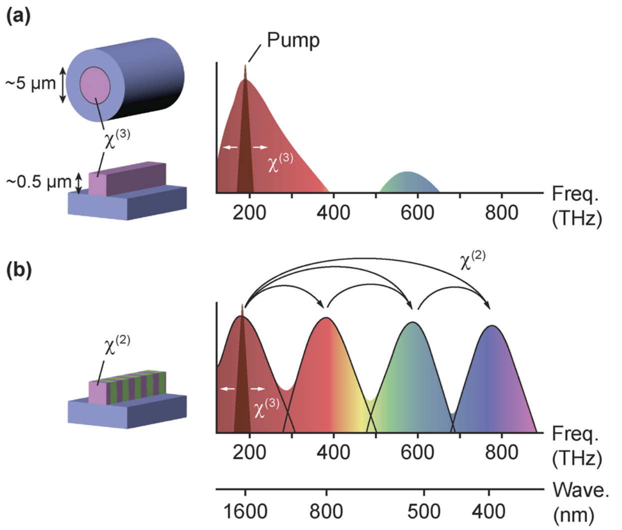

FIG. 1. Different supercontinuum (SC) generation platforms and their spectra. (a) Fiber- and nanophotonic waveguide-based SC generation with $\chi^{(3)}$ nonlinearity only. The generated spectrum features $\chi^{(3)}$ broadening around the pump and a small amount of third-harmonic generation. (b) $\chi^{(2)}$-based SC generation with $\chi^{(3)}$ broadening combined with $\chi^{(2)}$-based harmonics to generate a multi-octave-spanning spectrum.

broader spectra through harmonic generation [Fig. 1(b)]. These second-order processes are only efficient when the interacting waves are phase-matched. Although several phase-matching techniques are available for nanophotonic waveguides, including birefringent phase matching (BPM) and intermodal phase matching (IPM), quasi-phase matching (QPM) stands out among all as it not only offers exceptional SHG efficiencies[7,8] but also a design freedom for tuning the second-order effects over a broad spectral range. This tuning via QPM can help increase the efficiency of certain second-order processes over the others to effectively target a desired spectral region, or even complement conventional dispersion management by introducing an effective dispersion through QPM.[9] Second-order effects, such as SHG, can also provide practical benefits, such as carrier-envelope-offset frequency (f_{CEO}) detection via f–2f beatnotes (self-referencing), allowing for fully stabilized combs,[10] which are essential for precise metrology. Thus, nanophotonic waveguides with $\chi^{(2)}$ nonlinearity mark a significant progression in SC generation technology where phase-matched $\chi^{(2)}$ processes can be used for efficient spectral broadening and frequency conversion through harmonic generation [Fig. 1(b)].

Several nanophotonic material platforms can be utilized for nonlinear applications where $\chi^{(3)}$ and $\chi^{(2)}$ processes work in tandem, including aluminum nitride (AlN),[11,12] lithium niobate ($LiNbO_3$), gallium phosphide (GaP),[13] and more recently, gallium nitride (GaN).[14] Among these, thin-film lithium niobate, or lithium niobate-on-insulator (LNOI), is a powerful platform that not only has a strong $\chi^{(2)}$ coefficient but also allows for QPM with periodic poling. This provides the freedom to tailor second-order effects similar to the dispersion engineering for third-order effects. So far, several demonstrations have been made using periodically poled lithium niobate for broadband SC generation[15,16] including at high repetition rates.[17] While these developments showcase the immense potential of integrated photonic systems that harness second- and third-order nonlinear effects, they also highlight the critical need for fabrication capabilities that can reliably tailor the waveguide geometry and the phase-matching condition for a desired application.

Here, we present a fabrication process and experimental results for periodically poled, tightly confining LNOI waveguides, specifically designed for broadband SC generation into visible and ultraviolet (UV) wavelengths. Our fabrication features aperiodic (chirped) poling for broadband QPM and tight confinement via a fully etched lithium niobate layer. Our process is a path toward realizing the full potential of the SC generation using second- and third-order nonlinearities by allowing for a maximum degree of flexibility for the waveguide cross-section and realizing QPM by poling. The potential is demonstrated by the generation of SC spectra spanning multiple octaves that extend below 400 nm, also while operating at a high repetition rate.[18]

II. WAVEGUIDE FABRICATION

The fabrication of the periodically poled thin-film lithium niobate waveguides is illustrated in Fig. 2 in detail. As a substrate, we use a 4-in., x-cut LNOI wafer (NANOLN) with 800 nm $LiNbO_3$ layer on a 3 μm SiO_2 layer on bulk silicon (Si). Although the fabrication process presented in this section can be utilized at the wafer scale, we typically work with 16×16 mm dies. Before dicing the wafer into dies, platinum (Pt) alignment marks are defined across the wafer to ensure precise alignment of the poling electrodes and waveguides with the crystalline axes of the lithium niobate in the subsequent lithography steps. After dicing, the fabrication is performed on dies with three main steps: periodic poling, waveguide fabrication, and chip separation.

For the periodic poling step, first, chromium (Cr) surface electrodes are patterned via electron-beam lithography (EBL) using a methyl methacrylate (MMA)–poly(methyl methacrylate) (PMMA) bilayer and subsequent lift-off [Fig. 2(a)]. The poling electrodes are positioned 15 μm apart and are oriented such that the applied electric field is along the optical (crystalline z) axis of the crystal. The electrodes also feature tapered tips to provide a better electric field distribution and poling quality.[19] Second, periodic poling is performed by applying a high voltage (HV) across the electrodes [Fig. 2(c)] using a ferroelectric poling system (TF 3000, aixACCT) and an HV amplifier (Trek 2210, Advanced Energy). During the HV-poling process, the sample is covered in silicone (transformer) oil to prevent dielectric breakdown of the surrounding air. The HV signal applied for poling is shown in Fig. 2(e) and consists of two parts: The first part consists of three 1 ms long pulses at 300 V (20 V/μm) [Fig. 2(e)]. These pulses are often referred to as *pre-pulses* and have been shown to help nucleate domains closer to the positive electrode and facilitate further domain growth, yielding high-fidelity poled domains.[20] The second part (poling pulse) consists of a quick ramp to 450 V (30 V/μm) to propagate the nucleated domains to the negative (ground) electrode, followed by a slow voltage decay over 300 ms, to stabilize the inverted domains. During the poling process, the current is measured and integrated to calculate the charge

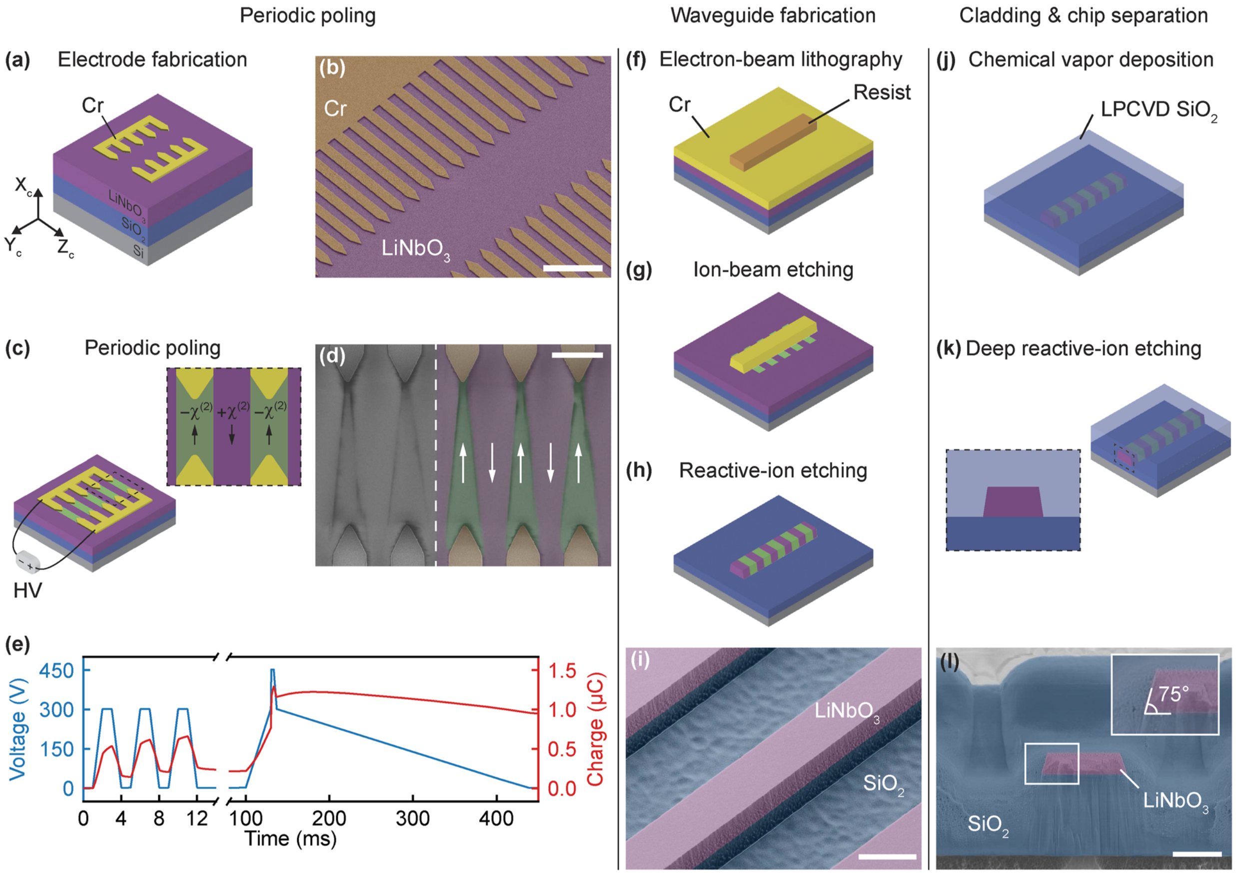

FIG. 2. Periodically poled lithium niobate waveguide fabrication. (a) Lithium niobate-on-insulator (LNOI) substrate with chromium (Cr) poling electrodes fabricated with electron-beam lithography (EBL) and lift-off. LiNbO$_3$ and SiO$_2$ layer thicknesses are 800 nm and 3 μm, respectively. (b) False-color scanning electron microscope (SEM) image of the Cr poling electrodes. The scale bar is 10 μm. (c) Illustration of periodic poling of lithium niobate. A high-voltage (HV) source is used to apply electric fields in excess of 21 V/μm (coercive field of LiNbO$_3$) to invert crystal domains periodically for quasi-phase matching (QPM). The small inset shows periodic sign change in second-order nonlinear susceptibility ($\chi^{(2)}$) as a result of the periodic poling. (d) Partially false-colored SEM image of the poled domains. The scale bar is 5 μm. (e) HV signal applied to the electrodes for poling. The domain nucleation is initiated with three 1 ms long pulses and the domain inversion is completed with a fast voltage ramp to 450 V (30 V/μm) and a slow decay over 300 ms. The charge is calculated by integrating the current over time. It provides a qualitative verification of the poling process. (f) EBL for patterning waveguides. Cr is used as a hard mask for high selectivity during reactive-ion etching (RIE). (g) Ion-beam etching (IBE) with argon (Ar) to transfer the electron-beam resist pattern to the Cr layer. The remaining resist is removed after etching. (h) RIE with fluorine chemistry to etch the lithium niobate layer. The remaining Cr is removed after etching and the sample is cleaned. (i) False-color SEM image of a through-etched waveguide after cleaning. The scale bar is 2 μm. (j) SiO$_2$ deposition as a 3 μm thick cladding layer via low-pressure chemical vapor deposition (LPCVD). (k) Series of RIE steps to reveal input and output facets. Individual etching steps are performed to remove all layers in sequence, including deep reactive-ion etching (DRIE) to remove the bulk silicon layer. (l) False-color SEM image of the input facet of a waveguide. The inset shows the through-etched waveguide layer with a 75° sidewall angle. The scale bar is 2 μm.

[Fig. 2(e)]. This provides an on-the-fly verification of the poling process, as the permanent increase in charge is due to the *remanent polarization*, i.e., the amount of polarization that remains in the material after the external field is removed, which is an indication of the inverted domains in ferroelectric crystals. However, it should be noted that this is a qualitative, rather than quantitative, measure for poling with surface electrodes [Fig. 2(a)], since relating the charge to the change in polarization requires knowing the precise volume between the electrodes where the polarization change occurs, which is difficult to estimate in this configuration, i.e., when the electrodes are co-planar.

After poling, the sample is inspected to verify the periodically poled domains across the substrate. Typical non-destructive inspection methods for visualizing ferroelectric domains in lithium niobate consist of either high-resolution serial methods such as piezoresponse force microscopy (PFM)[21,22] or diffraction-limited optical methods such as second-harmonic microscopy (SHM)[23] and polarization contrast microscopy (PCM).[20] In this work, we employ scanning electron microscopy (SEM). Although this is not a standard inspection method for ferroelectric domains, SEM strikes a good balance between resolution and acquisition time. While lithium niobate is an insulating material and the oppositely poled domains do not provide any contrast in SEM, the interface between oppositely polarized domains, or a domain wall (DW), is known to have higher conductivity compared to the bulk crystal,[24] thus allowing for reasonable contrast when an electron beam is scanned across the surface [Fig. 2(d)]. However, it should be noted that SEM is primarily a surface imaging technique, meaning that it provides information on periodically poled domains near the surface. Nevertheless, subsurface domains can theoretically be visualized by increasing the beam voltage, which allows for deeper electron penetration into the material.[25] After inspection, the Cr electrodes for poling are removed with chemical etching (TechniEtch Cr01, MicroChemicals GmbH) to prepare the samples for waveguide fabrication.

For waveguide fabrication, the etching method and the mask material play a crucial role. In addition to the performance characteristics such as propagation losses, they help define the waveguide cross-section and consequently the dispersion characteristics. Even though polymer[26] or inorganic resist masks such as hydrogen silsesquioxane (HSQ)[27] have been successfully used for fabricating high-Q resonators, they often have poor etch resistance when fluorine-based reactive-ion etching (RIE) is used to etch lithium niobate. This leads to a low etch selectivity (against lithium niobate) and limits the lithium niobate thicknesses that can be etched when resist masks are used. To mitigate this problem, etching can be made purely physical, i.e., only argon (Ar) sputtering, which will allow reasonable selectivity, but will result in shallow sidewalls of around 60°[28,29] and etching thick lithium niobate layers will require substantial resist thicknesses. Recently, higher sidewall angles of around 80° have been demonstrated in lithium niobate using Ar sputtering;[30,31] however, this process requires adjusting the incidence angle of Ar ions, a feature that is not available in most etching tools and can be limiting when etching negative patterns, i.e., small openings for resonators and couplers. Both of these properties, dictated by the etching process—the sidewall angle and the ability to etch thick lithium niobate films—become important when tight lateral confinement is needed either for compact integration or for subwavelength waveguiding structures (e.g., for mid-infrared (mid-IR) applications).

In contrast to resist masks, metal masks such as Cr or nickel (Ni) exhibit significant etch resistance to RIE with fluorine chemistry. Thus, they can be used as an etch mask to allow for the etching of relatively thick lithium niobate layers with better sidewall angles of around 75°.[32] Therefore, in this work, we use a Cr hard mask that we deposited using electron beam evaporation (EBE) and subsequently patterned with EBL [Fig. 2(f)] using a positive resist (ZEP520A, Zeon Corporation) and Ar ion beam etching (IBE) [Fig. 2(g)]. Then, RIE with fluorine chemistry (CHF_3/Ar) is used to transfer the hard mask pattern to the lithium niobate layer [Fig. 2(h)], resulting in a 75° sidewall angle [inset of Fig. 2(l)]. Finally, the remaining Cr is etched chemically, and waveguides are cleaned in Piranha solution (H_2SO_4:H_2O_2). The SEM image in Fig. 2(i) shows a waveguide made from a fully etched 800 nm thick lithium niobate layer on SiO_2. Although there is significant over-etching into the SiO_2 layer due to its poor etch resistance to CHF_3/Ar plasma, this will not significantly affect the waveguide performance, as these regions will later be buried under the SiO_2 cladding. This approach can easily be utilized to etch lithium niobate thicknesses in excess of 1 μm.

In the third and last fabrication step, the waveguides are cladded with a 3 μm thick SiO_2 layer using low-pressure chemical vapor deposition (LPCVD) [Fig. 2(j)]. Even though a SiO_2 cladding offers less index contrast ($n = 1.444$ at 1550 nm) compared to air ($n = 1$), it increases the longevity of the waveguides by protecting them from environmental factors and can improve both the coupling efficiency[33] and the power handling capability of the waveguides. It should also be noted that the SiO_2 layer is deposited at a relatively low temperature of 425 °C to preserve the periodically poled domains, as it has been shown that elevated temperatures can degrade the inverted domains.[34,35] After the cladding deposition, the waveguide facets are revealed through a series of RIE steps to separate four 5×5 mm photonic chips from the original die. This results in low roughness facets (compared to dicing), minimizing the scattering losses when coupling the light in and out.

III. WAVEGUIDE DESIGN

To experimentally validate the capabilities of the devices made using our process, we designed waveguides that target SC generation with maximum spectral coverage across both visible and UV wavelengths. This involves optimizing two nonlinear processes that take place sequentially in our waveguides: $\chi^{(3)}$-based spectral broadening and $\chi^{(2)}$-based harmonic generation. We strategically placed the spectral broadening before the harmonic generation stage as this should ensure the availability of the necessary frequency components for second-order processes and ultimately lead to a gap-free spectrum spanning several octaves through overlapping harmonics. The extent of $\chi^{(3)}$ spectral broadening depends on the group velocity dispersion (GVD) characteristics of the waveguides, which, in turn, is influenced by the waveguide geometry. On the other hand, the harmonic generation in the subsequent stage relies heavily on QPM, since the strong material dispersion of lithium niobate in the visible and UV wavelengths results in a phase mismatch that needs to be compensated for efficient second-order processes. Therefore, designing phase-matching structures for different $\chi^{(2)}$ processes is essential for harmonic generation and will be addressed here.

A. Waveguide geometry

Figure 3(a) illustrates the cross-section of a lithium niobate waveguide. Since the waveguide height (h) is determined by the film thickness of the substrate, the parameters we have control over are sidewall angle (θ), slab thickness (t_{slab}), and waveguide top width (w). Both θ and t_{slab} are determined by the etching process (method, chemistry, duration, etc.) and, therefore, are tunable between fabrication runs, though with certain limitations. Conversely, the waveguide top width (w) has the most freedom, as it is lithographically defined and can be varied within a photonic chip. Therefore, to determine the ideal waveguide geometry, we first performed a mode analysis for fundamental transverse electric (TE_{00}) mode using finite element modeling (FEM) software (COMSOL Multiphysics) to calculate the effective mode index as a function of wavelength. For the analysis, we considered two geometries: The first one, referred to as Design A [Fig. 3(b)], has $\theta = 60°$ and $t_{slab} = 300$ nm, representing typical fabrication capabilities when using resist masks, as discussed earlier. The second geometry, Design B in Fig. 3(c), represents the fabrication process detailed in Sec. II with $\theta = 75°$ and with no slab

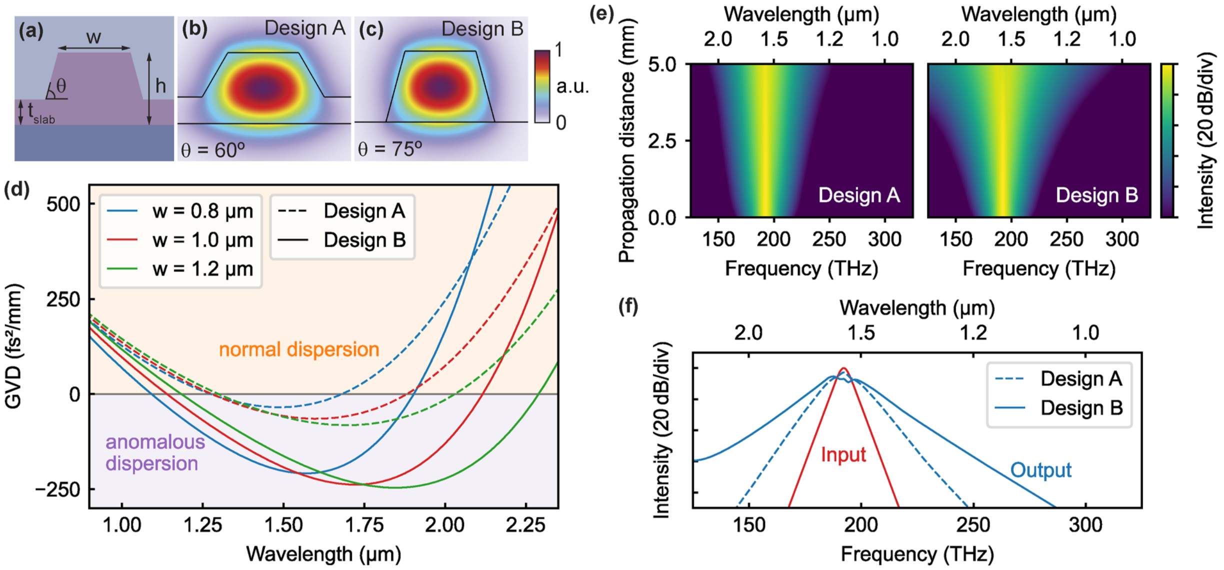

FIG. 3. Effect of the waveguide geometry on dispersion characteristics. (a) Illustration of a waveguide cross-section with different parameters. (b) Normalized electric field strength of the fundamental transverse electric (TE_{00}) mode for Design A with h = 0.8 μm, w = 0.8 μm, t_{slab} = 0.3 μm, and $\theta = 60°$. (c) Normalized electric field strength of the TE_{00} mode for Design B with h = 0.8 μm, w = 0.8 μm, t_{slab} = 0 (no slab), and $\theta = 75°$ (a.u.: arbitrary units). (d) Group velocity dispersion (GVD) of Design A and Design B for different waveguide top widths. (e) Numerical simulation (pychi)[36] results for Design A (left) and Design B (right) for spectral broadening with a 1560 nm input with pulse duration of 80 fs and pulse energy of 75 pJ. (f) Comparison of the simulated output spectra of two designs together with the input spectrum.

remaining (t_{slab} = 0). For both geometries, waveguide top width and optical frequency are varied. The GVD as a function of the wavelength for both geometries is shown in Fig. 3(d). Although a similar trend in GVD can be observed for both designs with increasing waveguide top width, Design B consistently offers larger anomalous dispersion values over a broader range of wavelengths, which are typically favorable for nonlinear applications such as SC generation and soliton formation. This is especially true for the 1.2 μm wide waveguide for which the dispersion is anomalous between the wavelengths of 1.2 and 2.3 μm.

To compare the spectral broadening of the two designs (Design A and Design B), we also performed numerical simulations using the open-source Python package *pychi*.[36] Here, the dispersion data that were previously calculated for both Design A and Design B with a waveguide top width of 0.8 μm are used. As an input, we define a pulsed input at 1560 nm with hyperbolic secant (sech) spectral distribution, pulse duration of 80 fs, and pulse energy of 75 pJ. The spectral broadening of both designs for a waveguide length of 5 mm can be seen in Fig. 3(e), along with the output spectra in Fig. 3(f). It is clear that Design B with larger anomalous dispersion can indeed result in a broader spectrum compared to Design A, especially into longer wavelengths, thus validating our design choice regarding waveguide cross-section.

B. Poling period

The second design step involves designing the QPM structures, that is, determining the poling (QPM) period required for relevant $\chi^{(2)}$ processes. In general, the QPM period is inversely proportional to the k-vector mismatch of the interacting waves. The QPM period for a generic three-wave process is

$$\Lambda_{\mathrm{QPM}} = \frac{2\pi}{\Delta k} = \frac{2\pi}{|k_1 + k_2 - k_3|}, \tag{1}$$

where k_1 and k_2 are the k-vectors of input waves, and k_3 is the k-vector of the output wave. The optimum QPM periods for a multitude of SFG processes such as SHG (where $k_1 = k_2$) are calculated from simulated dispersion data and shown in Fig. 4(a). The QPM period for SHG of 1560 nm is around 4.4 μm and does not vary significantly for wavelengths above 1250 nm. Indeed, for SHG, reasonable QPM bandwidths can be achieved with a fixed QPM period while mildly varying the waveguide width, or vice versa.[37,38] However, achieving broadband spectra through $\chi^{(2)}$ necessitates not only satisfying QPM requirements for multiple frequency pairs within an SFG process but also for a multitude of SFG processes such as SHG, third-harmonic generation (THG), and fourth-harmonic generation (FHG), which are indicated by different colored lines in Fig. 4(a). Achieving this is possible through chirped or aperiodic QPM designs, where the poling period is not constant, but rather varies along the propagation direction [Fig. 4(b)].

Another design consideration is related to the SFG processes which generate wavelengths in the visible and UV ranges. For these processes, the QPM period, Λ, drops significantly to around 1.2 μm due to strong dispersion. Achieving short QPM periods in the order of 1 μm (inverted domain width of 500 nm) is although possible,[21] challenging to realize with high spatial fidelity. The main problem stems from the lateral domain broadening during periodic poling, which prevents perfect 50:50 (both domains at equal

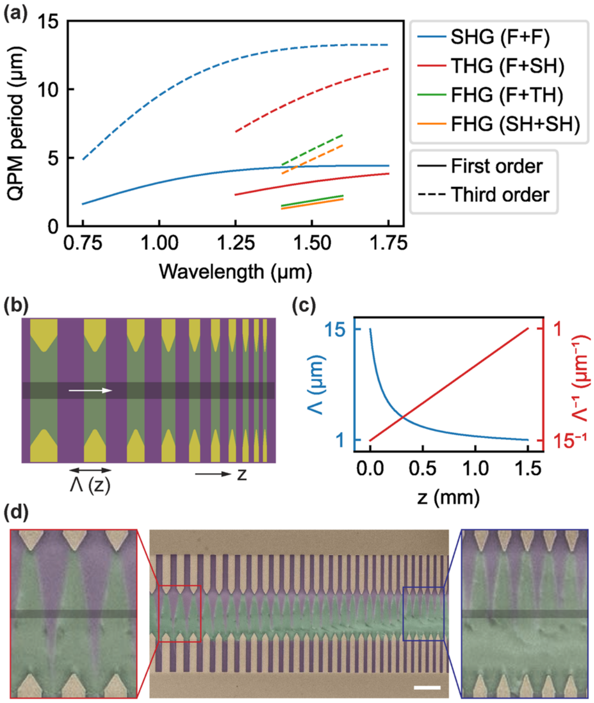

FIG. 4. Designing of the quasi-phase matching (QPM) pattern for lithium niobate waveguides. (a) QPM period as a function of fundamental wavelength for different second-order processes. Solid line indicates first-order phase-matching, whereas dashed lines are for higher (third-) order phase matching. Dispersion values of a waveguide with a top width of 1 µm are used in calculations. SHG: Second-harmonic generation, THG: Third-harmonic generation, FHG: Fourth-harmonic generation, F: Fundamental, SH: Second-harmonic, TH: Third-harmonic. (b) Illustration of chirped (aperiodic) poling for broadband QPM where the poling period is varied along the propagation direction. The dark-shaded region represents the waveguide; only one waveguide is placed in the center of the poled region. (c) Poling period (Λ) and spatial frequency of the poling period (Λ^{-1}) as a function of propagation distance for a 1.5 mm long waveguide section. (d) False-color scanning electron microscope (SEM) image of a lithium niobate sample with chirped poling. Both zoomed-in windows show 15 µm wide sections with varying poling periods. The dark-shaded regions indicate the waveguide placement in the poled region.

width) domain distribution. This leads to a drop in the QPM efficiency,[39] potentially preventing efficient harmonic generation into visible and UV wavelengths. To help alleviate this problem, higher order QPM can be utilized, where an odd-integer multiple, e.g., three for third-order QPM, of the QPM period can also satisfy the phase-matching condition [dashed lines in Fig. 4(a)]. This approach offers less peak efficiency for a given propagation length; however, fabrication requirements can be relaxed significantly. Therefore, in this work, we utilize a chirped (aperiodic) poling period (Λ) that spans from 15 to 1 µm. This range covers both first- and third-order phase-matching requirements for all relevant SFG processes for harmonic generation in the visible and UV wavelengths.

With the introduction of the chirped poling, the chirp rate, or function $\Lambda(z)$, becomes another design parameter that can be tailored to favor certain SFG processes, similar to choosing a poling period. Since the generated harmonic power will be determined, among other factors, by the phase-matched interaction length, we apply a chirp rate that allocates more space for shorter periods. This is done to allow for more first-order phase-matched interactions and compensate for previously mentioned inefficiencies regarding shorter poling periods. More specifically, rather than varying the poling period (Λ) linearly, we arbitrarily chose to design the chirp to be linear in spatial frequency of the period (Λ^{-1}). Our chirp function is

$$\Lambda(x)^{-1} = p_0^{-1}(1 - x) + p_1^{-1}x, \tag{2}$$

where x is a dimensionless variable for the normalized position along the poling length of L $(x = z/L)$. According to Eq. (2), the poling period $\Lambda(x)$ varies from p_0 for $x = 0$ $(z = 0)$ to p_1 for $x = 1$ $(z = L)$. Using this linear chirp rate in the spatial frequency (Λ^{-1}), more than 85% of the periodically poled region is allocated for first-order phase matching [1–5 µm, Fig. 4(a)] compared to only 29% with a linear chirp in poling period (Λ). The change in the poling period for $L = 1.5$ mm can be seen in Fig. 4(c). Figure 4(d) is a false-color SEM image that shows a poled lithium niobate sample with a changing poling period.

IV. EXPERIMENTAL VALIDATION

The broadband SC generation with the fabricated waveguides is reported in this section. We fabricated waveguides using the previously described process, resulting in waveguides with the geometric properties of Design B from Sec. III: a waveguide height of 0.8 µm, no slab $(t_{slab} = 0)$, and a sidewall angle of $\theta = 75^\circ$ [Fig. 2(l)]. The experimental setup used for testing is depicted in Fig. 5(a). As a source, we use a 100 MHz, 80 fs mode-locked laser with a central wavelength of 1560 nm. We couple the light into the waveguides using a polarization-maintaining (PM) lensed fiber with a specified mode field diameter (MFD) of 2.5 µm. The waveguide top width (w) at the input and output facets is 2.5 µm [Fig. 2(l)] and tapered to the waveguide width in 0.25 mm long sections. Using these edge couplers for both input and output, we measured a total transmission efficiency (output to input power fraction, including propagation losses) of 19% (−7.2 dB) on average at 1550 nm. We expect this value to be dominated by the coupling losses, given the relatively short propagation length of the waveguides (5 mm). The average output power of the laser is set to 100 mW, corresponding to a pulse energy of 1 nJ. Based on the transmission measurements and the additional losses leading to the waveguide, we estimate the on-chip pulse energy to be ~300 pJ. The total waveguide length is 5 mm and, excluding the coupling tapers, the remaining length of 4.5 mm is designed with two sections: a 3 mm long spectral broadening section (without poling) followed by a 1.5 mm long periodically poled section with a chirped period from 15 to 1 µm. After the waveguide, the spectra are collected using a large-core (100 µm), fluoroindate (InF_3) multimode (MM) fiber to minimize UV absorption losses and ensure that no further nonlinear effects take place in the fiber after the light is collected. Later, the spectra are recorded using an optical spectrum analyzer (OSA) (AQ6374, Yokogawa).

A photograph of one of the waveguides during operation is shown in Fig. 5(b). Here, individual stages of SC generation can be identified clearly from the scattered light. In the first 3 mm of the waveguide, which is used for spectral broadening, only a weak visible light is scattered from the waveguide, as most of the optical power still resides in the infrared (IR) region. However, soon after the start

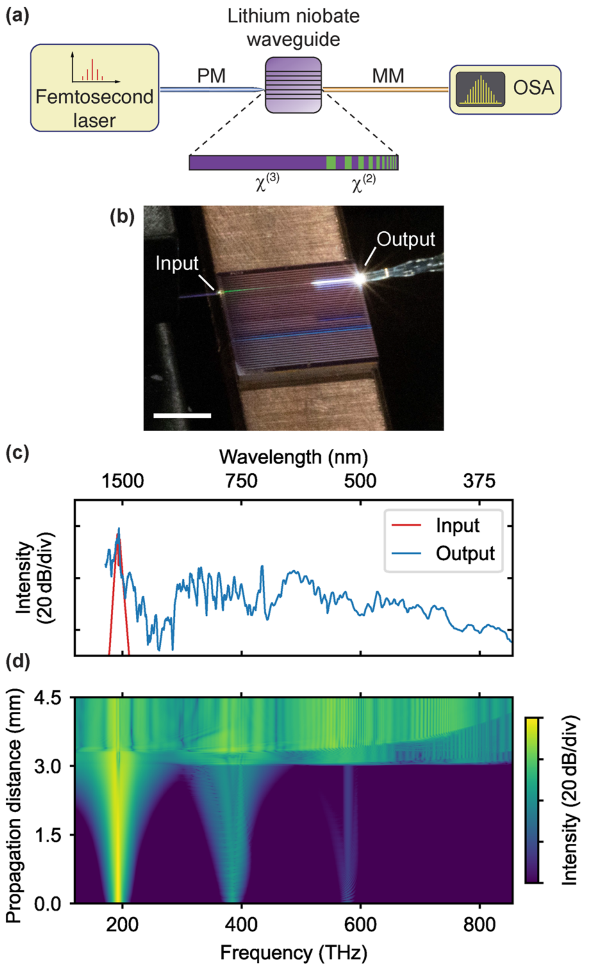

FIG. 5. Broadband supercontinuum (SC) generation using a periodically poled lithium niobate waveguide. (a) Experimental setup. The input is a 100 MHz, 80 fs mode-locked laser at a central wavelength of 1560 nm and an average power of 100 mW (pulse energy of 1 nJ). The laser output is coupled into the waveguide using a polarization-maintaining (PM) lensed fiber with a specified mode field diameter (MFD) of 2.5 μm. The output light is collected using a fluoroindate (InF_3) multimode (MM) optical fiber to minimize ultraviolet (UV) absorption and recorded using an optical spectrum analyzer (OSA). (b) Photograph of the waveguide during SC generation. The periodically poled $\chi^{(2)}$ section close to the output can be identified by the scattered white light. Scale bar is 2 mm. (c) Recorded output light of a waveguide with a top width of 0.8 μm. The resulting spectrum spans multiple octaves and is limited only by the detection window of the OSA. (d) Numerical simulation results of the same waveguide in (c) for a length of 4.5 mm consisting of 3 mm long $\chi^{(3)}$ and 1.5 mm long $\chi^{(2)}$ section. The input pulse is centered at 1560 nm, and pulse duration and energy are 80 fs and 300 pJ, respectively.

of the periodically poled section, scattered light becomes "white," indicating the harmonic generation of visible wavelengths. This can also be seen from the nonlinear simulation results in Fig. 5(d), where, in the first 3 mm of the waveguide, a broadened input comb and a weak second harmonic are observed. However, in the periodically poled section, phase-matched $\chi^{(2)}$ processes generate light in the visible and UV ranges, similar to the observation from Fig. 5(b).

The measured output spectrum from a waveguide with a top width of 0.8 μm is shown in Fig. 5(c). Here, we can see the gap-free spectrum spanning several octaves, from 150 to 850 THz, only limited by the detection window of the OSA. We also observed, across multiple waveguides, a general decrease in the light intensity starting from longer wavelengths of the visible spectrum to blue and UV. We attribute this trend to several factors: First, the visible and UV wavelengths are generated through cascaded $\chi^{(2)}$ processes where multiple processes take place in sequence. Therefore, any inefficient process will affect the subsequent processes that rely on it, compounding the effect. Second, as mentioned before, generating lower wavelengths typically requires small QPM periods due to strong material dispersion [Fig. 4(a)], thus prone to inefficiencies related to duty-cycle errors in poling. An example of this can be seen in Fig. 4(d), where the deviation from the ideal 50% duty cycle for alternating domains is more severe for smaller QPM periods compared to larger ones.

In a different test, we investigated how different design choices affect the output spectra. To do this, we used waveguides with a similar configuration as before (3 mm spectral broadening section, 1.5 mm periodically poled section), yet with different chirp directions. In one design, the poling period is chirped down from 15 to 1 μm with a chirp rate indicated in Eq. (2), whereas in another waveguide, the poling period is chirped up from 1 to 15 μm with the same chirp rate. The output spectra for both of these waveguides are shown in Figs. 6(a) and 6(b). In both designs, broadband, gap-free spectrum is generated with similar spectral features, indicating

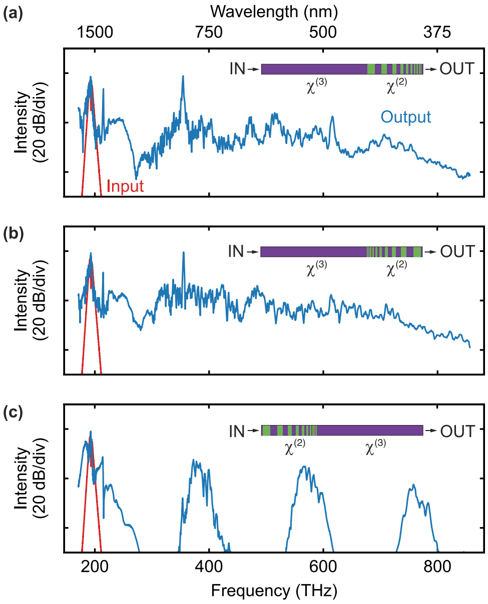

FIG. 6. Output spectra of different waveguide configurations with (a) chirped down $\chi^{(2)}$ section (15 to 1 μm) after the $\chi^{(3)}$ section, (b) chirped up $\chi^{(2)}$ section (1–15 μm) after the $\chi^{(3)}$ section and (c) same waveguide as in (b) when the propagation direction changed. The waveguide top width is 2.5 μm for all waveguides and the input comb is shown with the red line in all plots. Configurations in (a) and (b) result in similar spectra, whereas the waveguide in (c) shows significantly different behavior with less broad harmonics due to depletion of the peak pulse power.

that the spectral broadening, specifically the harmonic generation, is mostly insensitive to the chirp direction.

In contrast, when the propagation direction is varied for the same waveguide in Fig. 6(b) by switching the input and the output, the resulting spectrum is strikingly different. Since, in this configuration, the periodically poled section comes before the broadening section, the phase-matched interactions give way to harmonics before the input IR comb is broadened enough. Consequently, peak power is lost to the harmonics early on, and the pulse stretches in time, leading to limited broadening of the IR comb in the spectral broadening section. In addition to this, due to strong normal dispersion in lower wavelengths [Fig. 3(a)], there is no spectral broadening of the harmonics, thus, leading to a less broad spectrum overall.

V. DISCUSSION

Recent advancements in integrated lithium niobate photonics have unlocked new possibilities for harnessing nonlinear effects, enabling wavelength conversion and the generation of coherent and quantum light sources, even at wavelengths where no laser gain media exist. In this work, we present a fabrication method for creating periodically poled waveguides from relatively thick lithium niobate films—thicker than those typically used—and with variable etch depths, including fully etched structures. This approach enables the realization of high-confinement, nanoscale periodically poled lithium niobate waveguides that generate multi-octave-spanning spectra, extending into visible and UV wavelengths from a near-infrared (near-IR) source, by leveraging both second- and third-order nonlinear effects.

Our experimental results align with other recent studies that utilize second-order effects to achieve a broad visible spectrum,[17] including one that demonstrated similar spectral coverage using thin-film lithium niobate.[16] However, while our optical demonstration shares a similar approach in design and implementation, and the experimental supercontinuum spectra also exhibit extremely broadband coverage, the fabrication method described here in detail allows for more flexible waveguide cross-sections. In particular, the deep-etched lithium niobate waveguides demonstrated here offer enhanced control of the tighter mode confinement and better dispersion characteristics [Fig. 3(d)] compared to conventional and commonly practiced fabrication approaches mentioned earlier and also used in said work.

We believe that the generated spectra are not only limited to what we demonstrate in this work. Even though we did not measure the spectrum at longer wavelengths, it is highly likely that the generated harmonics will also seed DFG processes that can extend the spectrum well into the mid-IR range. Indeed, deep-etched lithium niobate waveguides demonstrated in this work not only imply better dispersion and nonlinear characteristics but are also important for providing the stronger confinement needed for longer wavelengths. Together with the tunability of the second-order effects offered by QPM, efficient SFG and DFG processes can help generate comb sources that span the entire transmission range of lithium niobate, from 350 nm until ~5000 nm.

To reach the full potential of this platform, several performance characteristics need improvement. First, increasing the coupling efficiency is extremely important for increasing the on-chip power for nonlinear processes, especially for high-repetition-rate sources, where available pulse energies are constrained due to high average powers.[18] This can be achieved by optimizing the design of the edge couplers and incorporating inverse tapers.[33,40] Second, low-loss propagation over a very wide spectral range can also be ensured by minimizing the sidewall roughness either through optimizing the lithium niobate etching process,[31,41] or by post-etch cleaning and treatment.[42,43] There is also growing interest in various SiO_2 cladding deposition methods and post-treatments, such as annealing, to reduce absorption losses in the near- and mid-IR,[44,45] which can be instrumental for broadband frequency sources. In addition to reducing losses, improving the periodic poling of lithium niobate can result in higher fidelity domains, further enhancing the efficiency of second-order processes. Optimized QPM designs can also facilitate more complex, cascaded nonlinear processes.

As a generic nonlinear photonic platform, our fabrication process can be used for many other integrated photonic applications beyond SC generation. In particular, applications that require high nonlinearities would benefit from the presented results, such as optical parametric oscillators (OPO), wavelength conversion of continuous-wave (CW) light in metrology and datacom/telecom or in quantum applications such as quantum networks or repeaters.

ACKNOWLEDGMENTS

This project received funding from the Swiss National Science Foundation (Grant No. CRSII5_193689), the EU Horizon 2020 research and innovation program (ERC StG 853564), and the Helmholtz Young Investigators Group VH-NG-1404. The work was supported through the Maxwell computational resources operated at DESY. Fabrication of the lithium niobate waveguides was carried out at the Center of MicroNanoTechnology (CMi) at EFPL. Periodic poling of the lithium niobate samples presented here was partially carried out at the Swiss Center for Electronics and Microtechnology (CSEM). The authors acknowledge the support of the BLUVES (BLue to UV Extreme precision astronomical Spectroscopy) consortium and the Advanced Nano Electromechanical Systems (ANEMS) laboratory at EPFL in this work. The authors would like to thank Dr. Cristina Martin Olmos for her support on SEM imaging of periodically poled lithium niobate samples.

AUTHOR DECLARATIONS

Conflict of Interest

The authors have no conflicts to disclose.

Author Contributions

Furkan Ayhan: Conceptualization (equal); Investigation (equal); Resources (lead); Writing – original draft (lead). **Markus Ludwig**: Conceptualization (equal); Investigation (equal); Resources (supporting); Writing – review & editing (supporting). **Tobias Herr**: Conceptualization (equal); Supervision (supporting); Writing – review & editing (supporting). **Victor Brasch**: Conceptualization (equal); Supervision (lead); Writing – review & editing (supporting). **Luis Guillermo Villanueva**: Conceptualization (equal); Supervision (lead); Writing – review & editing (supporting).

DATA AVAILABILITY

The data that support the findings of this study are available from the corresponding author upon reasonable request.

REFERENCES

[1] R. R. Alfano and S. L. Shapiro, "Emission in the region 4000 to 7000 Å via four-photon coupling in glass," Phys. Rev. Lett. **24**, 584 (1970).

[2] R. R. Alfano and S. L. Shapiro, "Observation of self-phase modulation and small-scale filaments in crystals and glasses," Phys. Rev. Lett. **24**, 592 (1970).

[3] J. K. Ranka, R. S. Windeler, and A. J. Stentz, "Visible continuum generation in air–silica microstructure optical fibers with anomalous dispersion at 800 nm," Opt. Lett. **25**, 25–27 (2000).

[4] W. H. Reeves, D. V. Skryabin, F. Biancalana, J. C. Knight, P. S. J. Russell, F. G. Omenetto, A. Efimov, and A. J. Taylor, "Transformation and control of ultra-short pulses in dispersion-engineered photonic crystal fibres," Nature **424**, 511–515 (2003).

[5] J. M. Dudley and J. R. Taylor, "Ten years of nonlinear optics in photonic crystal fibre," Nat. Photonics **3**, 85–90 (2009).

[6] C.-S. Brès, A. Della Torre, D. Grassani, V. Brasch, C. Grillet, and C. Monat, "Supercontinuum in integrated photonics: Generation, applications, challenges, and perspectives," Nanophotonics **12**, 1199–1244 (2023).

[7] J. Lu, J. B. Surya, X. Liu, A. W. Bruch, Z. Gong, Y. Xu, and H. X. Tang, "Periodically poled thin-film lithium niobate microring resonators with a second-harmonic generation efficiency of 250 000%/W," Optica **6**, 1455–1460 (2019).

[8] P.-K. Chen, I. Briggs, C. Cui, L. Zhang, M. Shah, and L. Fan, "Adapted poling to break the nonlinear efficiency limit in nanophotonic lithium niobate waveguides," Nat. Nanotechnol. **19**, 44–50 (2024).

[9] M. A. Arbore, A. Galvanauskas, D. Harter, M. H. Chou, and M. M. Fejer, "Engineerable compression of ultrashort pulses by use of second-harmonic generation in chirped-period-poled lithium niobate," Opt. Lett. **22**, 1341–1343 (1997).

[10] E. Obrzud, S. Denis, H. Sattari, G. Choong, S. Kundermann, O. Dubochet, M. Despont, S. Lecomte, A. H. Ghadimi, and V. Brasch, "Stable and compact RF-to-optical link using lithium niobate on insulator waveguides," APL Photonics **6**, 121303 (2021).

[11] X. Liu, A. W. Bruch, J. Lu, Z. Gong, J. B. Surya, L. Zhang, J. Wang, J. Yan, and H. X. Tang, "Beyond 100 THz-spanning ultraviolet frequency combs in a non-centrosymmetric crystalline waveguide," Nat. Commun. **10**, 2971 (2019).

[12] J. Lu, X. Liu, A. W. Bruch, L. Zhang, J. Wang, J. Yan, and H. X. Tang, "Ultraviolet to mid-infrared supercontinuum generation in single-crystalline aluminum nitride waveguides," Opt. Lett. **45**, 4499–4502 (2020).

[13] M. Rutkauskas, A. Srivastava, and D. T. Reid, "Supercontinuum generation in orientation-patterned gallium phosphide," Optica **7**, 172–175 (2020).

[14] W. Fan, M. Ludwig, I. Rousseau, I. Arabadzhiev, B. Ruhnke, T. Wildi, and T. Herr, "Supercontinua from integrated gallium nitride waveguides," Optica **11**, 1175–1181 (2024).

[15] K. Iwakuni, S. Okubo, O. Tadanaga, H. Inaba, A. Onae, F.-L. Hong, and H. Sasada, "Generation of a frequency comb spanning more than 3.6 octaves from ultraviolet to mid infrared," Opt. Lett. **41**, 3980–3983 (2016).

[16] T.-H. Wu, L. Ledezma, C. Fredrick, P. Sekhar, R. Sekine, Q. Guo, R. M. Briggs, A. Marandi, and S. A. Diddams, "Visible-to-ultraviolet frequency comb generation in lithium niobate nanophotonic waveguides," Nat. Photonics **18**, 218–223 (2024).

[17] Y. S. Cheng, K. Dadi, T. Mitchell, S. Thompson, N. Piskunov, L. D. Wright, C. B. A. Gawith, R. A. McCracken, and D. T. Reid, "Continuous ultraviolet to blue-green astrocomb," Nat. Commun. **15**, 1466 (2024).

[18] M. Ludwig, F. Ayhan, T. M. Schmidt, T. Wildi, T. Voumard, R. Blum, Z. Ye, F. Lei, F. Wildi, F. Pepe *et al.*, "Ultraviolet astronomical spectrograph calibration with laser frequency combs from nanophotonic lithium niobate waveguides," Nat. Commun. **15**, 7614 (2024).

[19] B. J. Stanicki, M. Younesi, F. J. F. Löchner, H. Thakur, W.-K. Chang, R. Geiss, F. Setzpfandt, Y.-H. Chen, and T. Pertsch, "Surface domain engineering in lithium niobate," OSA Continuum **3**, 345–358 (2020).

[20] M. Younesi, R. Geiss, S. Rajaee, F. Setzpfandt, Y.-H. Chen, and T. Pertsch, "Periodic poling with a micrometer-range period in thin-film lithium niobate on insulator," J. Opt. Soc. Am. B **38**, 685–691 (2021).

[21] J. T. Nagy and R. M. Reano, "Submicrometer periodic poling of lithium niobate thin films with bipolar preconditioning pulses," Opt. Mater. Express **10**, 1911–1920 (2020).

[22] B. Gautier and V. Bornand, "Nanoscale observation of the distribution of the polarization orientation of ferroelectric domains in lithium niobate thin films," Thin Solid Films **515**, 1592–1596 (2006).

[23] M. Rüsing, J. Zhao, and S. Mookherjea, "Second harmonic microscopy of poled x-cut thin film lithium niobate: Understanding the contrast mechanism," J. Appl. Phys. **126**, 114105 (2019).

[24] M. Schröder, A. Haußmann, A. Thiessen, E. Soergel, T. Woike, and L. M. Eng, "Conducting domain walls in lithium niobate single crystals," Adv. Funct. Mater. **22**, 3936–3944 (2012).

[25] L. S. Kokhanchik, R. V. Gainutdinov, S. D. Lavrov, and T. R. Volk, "Characteristics of microdomains and microdomain patterns recorded by electron beam irradiation on Y-cut $LiNbO_3$ crystals," J. Appl. Phys. **118**, 072001 (2015).

[26] Y. Gao, F. Lei, M. Girardi, Z. Ye, R. Van Laer, V. Torres-Company, and J. Schröder, "Compact lithium niobate microring resonators in the ultrahigh Q/V regime," Opt. Lett. **48**, 3949–3952 (2023).

[27] X. Zhu, Y. Hu, S. Lu, H. K. Warner, X. Li, Y. Song, L. Magalhães, A. Shams-Ansari, A. Cordaro, N. Sinclair *et al.*, "Twenty-nine million intrinsic Q-factor monolithic microresonators on thin-film lithium niobate," Photonics Res. **12**, A63–A68 (2024).

[28] M. Yu, B. Desiatov, Y. Okawachi, A. L. Gaeta, and M. Lončar, "Coherent two-octave-spanning supercontinuum generation in lithium-niobate waveguides," Opt. Lett. **44**, 1222–1225 (2019).

[29] L. Cai, A. Mahmoud, and G. Piazza, "Low-loss waveguides on Y-cut thin film lithium niobate: Towards acousto-optic applications," Opt. Express **27**, 9794–9802 (2019).

[30] Z. Li, R. N. Wang, G. Lihachev, J. Zhang, Z. Tan, M. Churaev, N. Kuznetsov, A. Siddharth, M. J. Bereyhi, J. Riemensberger, and T. J. Kippenberg, "High density lithium niobate photonic integrated circuits," Nat. Commun. **14**, 4856 (2023).

[31] F. Kaufmann, G. Finco, A. Maeder, and R. Grange, "Redeposition-free inductively-coupled plasma etching of lithium niobate for integrated photonics," Nanophotonics **12**, 1601–1611 (2023).

[32] I. Krasnokutska, J.-L. J. Tambasco, X. Li, and A. Peruzzo, "Ultra-low loss photonic circuits in lithium niobate on insulator," Opt. Express **26**, 897–904 (2018).

[33] L. He, M. Zhang, A. Shams-Ansari, R. Zhu, C. Wang, and M. Lončar, "Low-loss fiber-to-chip interface for lithium niobate photonic integrated circuits," Opt. Lett. **44**, 2314–2317 (2019).

[34] M. Yamada and M. Saitoh, "Fabrication of a periodically poled laminar domain structure with a pitch of a few micrometers by applying an external electric field," J. Appl. Phys. **84**, 2199–2206 (1998).

[35] H. Zhang, H. Zhu, Q. Li, and H. Hu, "Reversed domains in x-cut lithium niobate thin films," Opt. Mater. **109**, 110364 (2020).

[36] T. Voumard, M. Ludwig, T. Wildi, F. Ayhan, V. Brasch, L. G. Villanueva, and T. Herr, "Simulating supercontinua from mixed and cascaded nonlinearities," APL Photonics **8**, 036114 (2023).

[37] K. Mizuuchi, K. Yamamoto, M. Kato, and H. Sato, "Broadening of the phase-matching bandwidth in quasi-phase-matched second-harmonic generation," IEEE J. Quantum Electron. **30**, 1596–1604 (1994).

[38] A. Tehranchi and R. Kashyap, "Design of novel unapodized and apodized step-chirped quasi-phase matched gratings for broadband frequency converters based on second-harmonic generation," J. Lightwave Technol. **26**, 343–349 (2008).

[39] M. M. Fejer, G. A. Magel, D. H. Jundt, and R. L. Byer, "Quasi-phase-matched second harmonic generation: Tuning and tolerances," IEEE J. Quantum Electron. **28**, 2631–2654 (1992).

[40] C. Hu, A. Pan, T. Li, X. Wang, Y. Liu, S. Tao, C. Zeng, and J. Xia, "High-efficient coupler for thin-film lithium niobate waveguide devices," Opt. Express **29**, 5397–5406 (2021).

[41] CH. S. S. Kumar, N. N. Klimov, and P. S. Kuo, "Optimization of waveguide fabrication processes in lithium-niobate-on-insulator platform," AIP Adv. **14**, 065317 (2024).

[42] G. Ulliac, V. Calero, A. Ndao, F. I. Baida, and M.-P. Bernal, "Argon plasma inductively coupled plasma reactive ion etching study for smooth sidewall thin film lithium niobate waveguide application," Opt. Mater. **53**, 1–5 (2016).

[43] S. Y. Siew, E. J. H. Cheung, H. Liang, A. Bettiol, N. Toyoda, B. Alshehri, E. Dogheche, and A. J. Danner, "Ultra-low loss ridge waveguides on lithium niobate via argon ion milling and gas clustered ion beam smoothening," Opt. Express **26**, 4421–4430 (2018).

[44] A. Shams-Ansari, G. Huang, L. He, Z. Li, J. Holzgrafe, M. Jankowski, M. Churaev, P. Kharel, R. Cheng, D. Zhu *et al.*, "Reduced material loss in thin-film lithium niobate waveguides," APL Photonics **7**, 081301 (2022).

[45] Z. Qiu, Z. Li, R. N. Wang, X. Ji, M. Divall, A. Sidharth, and T. J. Kippenberg, "Hydrogen-free low-temperature silica for next generation integrated photonics," arXiv:2312.07203 (2023).